An empirical model of the occurrence rate of low latitude post-sunset plasma irregularities derived from CHAMP and Swarm magnetic observations

C. Stolle[1], T. A. Siddiqui[1], L. Schreiter[2,3], S. K. Das[1], I. Rusch[1], M. Rother[3]

[1]Leibniz Institute of Atmospheric Physics at the University of Rostock, Kühlungsborn, Germany
[2] Institute of Geodesy, Technical University of Berlin, Germany
[3]GFZ German Research Centre for Geosciences, Helmholtz Centre Potsdam, Germany

Key Points:

- The IBP model to estimate the occurrence probability of post-sunset equatorial plasma depletions (EPDs) is introduced.
- IBP shows high performance in predicting EPD occurrence for longitude, local time, day of year, solar activity, at altitudes of 350-500 km.
- The IBP model is publicly available including documentation.

Corresponding author: Claudia Stolle, `cstolle@iap-kborn.de`

Abstract

The prediction of post-sunset equatorial plasma depletions (EPDs), often called ionospheric plasma bubbles, has remained a challenge for decades. In this study, we introduce the Ionospheric Bubble Probability (IBP), an empirical model to predict the occurrence probability of EPDs derived from 9 years of CHAMP and 8.5 years of Swarm magnetic field measurements. The model predicts the occurrence probability of EPDs for a given longitude, day of year, local time and solar activity, for the altitude range 350-500 km, and low geographic latitudes of $\pm$ 45°. IBP has been found to successfully reconstruct the distribution of EPDs as reported in previous studies from independent data. IBP has been further evaluated using one-year of partly untrained data of the Ionospheric Bubble Index (IBI). IBI is a Level 2 product of the Swarm satellite mission used for EPD identification. The relative operating characteristics (ROC) curve shows positive excursion above the no-skill line with Hanssen and Kuiper's Discriminant (H&KSS) score of 0.66, 0.73, and 0.65 at threshold model outputs of 0.22, 0.18, and 0.18 for Swarm A, B, and C satellites, respectively. Additionally, the reliability plots show proximity to the diagonal line with a fairly decent Brier Skill Score (BSS) of 0.317, 0.320, and 0.316 for Swarm A, B, and C respectively. These tests indicate that the model performs significantly better than a no-skill forecast. The IBP model offers a compelling glimpse into the future of EPD forecasting, thus demonstrating its potential to reliably predict EPD occurrences. The IBP model is made publicly available.

Plain Language Summary

[Post-sunset equatorial plasma depletions (EPDs), often called ionospheric plasma bubbles, are a severe threat for reliable radio wave communication. However, their predictability has remained a challenge for the scientific community for decades. In this study, we introduce the Ionospheric Bubble Probability (IBP) model predicting the occurrence probability of post-sunset EPDs for a given longitude, day of year, local time and solar activity, for the altitude range 350-500 km, and low geographic latitudes of $\pm$ 45°. To this aim we have used 9 years of CHAMP and 8.5 years of Swarm magnetic field measurements. The IBP model predictions have been found to agree well with climatologies derived from independent data and performs largely better than unskilled forecasts. The IBP model is made publicly available.]

1 Introduction

The post-sunset equatorial and low-latitude ionosphere is susceptible to irregularities associated with F region plasma instability, popularly known as equatorial plasma depletions (EPDs) or ionospheric plasma bubbles. EPDs are regions of steep plasma depletions of several orders of magnitude in electron density with scale sizes ranging from thousands of kilometers down to meters (e.g., D. L. Hysell & Seyler, 1998; Lühr et al., 2014; Su et al., 2001). EPD is believed to be governed by the Rayleigh-Taylor (RT) instability mechanism which operates at the bottomside F region when uplifted during evening time post-sunset rise driven by the pre-reversal enhancement (PRE) of zonal electric field over the dip equator (e.g., Balsley et al., 1972; Haerendel, 1973; Ossakow, 1981; Sultan, 1996; Woodman & La Hoz, 1976; Tsunoda, 2005). The growth of RT instability depends on various ionospheric and thermospheric parameters which include F layer height, zonal (eastward) electric field, bottomside density gradient, meridional wind and perturbation in electron density in the form of seed (e.g., Kelley, 2009). EPDs have been found to exhibit serious threats to radio waves employed for satellite-based communication/navigation applications by producing random fluctuations in signal amplitude and phase known as scintillations. Based on simultaneous observations of plasma density and Global Positioning System (GPS) observables on board the Swarm satellite mission, Xiong et al. (2016, 2020) showed the positive relation between the strengths of EPDs and the severeness of

GPS scintillations to even total signal losses. Therefore, predicting EPD occurrence is of absolute necessity.

Although the underlying principle of RT instability is well understood (e.g., Kelley, 2009; Sultan, 1996), understanding the variability in EPD occurrence on a day-to-day basis continues to be puzzling (e.g., Abdu, 2019; Basu et al., 2009; Carter et al., 2014; Chou et al., 2020; Manju & Aswathy, 2020; Rajesh et al., 2017; Retterer & Roddy, 2014; Saito & Maruyama, 2007; Shinagawa et al., 2018; Tsunoda et al., 2010, 2018; Yamamoto et al., 2018; Das et al., 2021; D. L. Hysell et al., 2022; Patra & Das, 2023). While the PRE has been found to show a remarkable agreement with EPD occurrence climatologically (e.g., Clemesha & Wright, 1966; Dabas et al., 2003; Fejer et al., 1999; Gentile et al., 2006b; D. Hysell & Burcham, 2002; Stolle et al., 2008; Su et al., 2008; Tsunoda, 2005; Huang & Hairston, 2015), it fails to account on its day-to-day occurrence variability (e.g., Abdu et al., 1983; Fukao et al., 2006; Saito & Maruyama, 2006, 2007). Intriguingly, the growth rate of RT instability has been found to display similar uncertainty (e.g., Shinagawa et al., 2018; Das et al., 2021; Aa et al., 2023). Since the EPD occurrence shows a large variability both in small- and large-longitudinal scales (e.g., Kil et al., 2009; Kil & Heelis, 1998a; Martinis et al., 2021; Singh et al., 1997; Stolle et al., 2008; Tsunoda et al., 2018; Tsunoda & White, 1981), predicting EPD occurrence becomes even more challenging. Now, it is fairly well understood that missing understanding of the spatio-temporal behaviour of EPDs, i.e. growth, zonal movement and decay of EPDs, along with the paucity of continuous measurements of ionospheric parameters is the cause for the challenge in predicting the day-to-day occurrence variability of EPDs (e.g., Das et al., 2021; Li et al., 2021; D. L. Hysell et al., 2021; Patra & Das, 2023).

While for a long time, traditional methods such as in situ density measurements, optical imagers and radio wave sounding have been employed to study the day-to-day, global, and climatological occurrence of EPDs (e.g., Woodman & La Hoz, 1976; Farley et al., 1970; Kudeki & Bhattacharyya, 1999; Sahai et al., 1994, 2000; Kil & Heelis, 1998b; Fagundes et al., 1999; Burke et al., 2004; Gentile et al., 2011; Huang et al., 2014; Martinis & Mendillo, 2007; Das et al., 2021; Aa et al., 2023), subsequently, it has been found that magnetic field perturbations associated with the diamagnetic current linked to steep density gradient at the edges of the EPDs can also be used for characterizing EPDs (e.g., Lühr et al., 2002; Rodríguez-Zuluaga et al., 2019). Diagnosing EPDs through those signatures in the magnetic field and electron density, Stolle et al. (2006) could successfully reconstruct the well-known EPB climatology using Flux-Gate Magnetometer (FGM) measurements on-board the Challenging Mini-Satellite Payload (CHAMP) which similarly were obtained by traditional methods based on plasma density data from other satellite missions (e.g., Gentile et al., 2006b; Xiong et al., 2010). This success led to the introduction of the Ionospheric Bubble Index (IBI) as a standard Level 2 (L2) data product of the Swarm mission for the detection of EPDs (e.g., Park et al., 2013). Recently, Reddy et al. (2023) have utilized a machine learning (ML) based AI Prediction of EPBs (APE) model to predict the IBI. Their model is derived from 8 years of Swarm data. Feature analyses revealed that F10.7 is the most important feature in driving the EPB predictions, whereas latitude is the least.

The advantage of EPD climatology derived from in situ observations of polar-orbiting, Low Earth Orbit (LEO) satellites is their global coverage. However, it should be noted that these satellites can only detect those irregularities that have evolved into plumes reaching F region altitudes at or above the F2 peak. Conversely, the bottom-side F region irregularities, from which plumes may evolve, occur more frequently than F region plumes are observed, e.g., almost every evening throughout the year and solar cycle, e.g., in the American sector. A comprehensive investigation of the irregularity occurrence derived from 20 years of incoherent scatter radar data at the Jicamarca radio observatory has been provided by Zhan et al. (2018). Accordingly, based on 10 years of ground-based GPS observations distributed in South America, Macho et al. (2022) indicated some activity of weak scintillations also during low solar flux years, while moderate or intense scintillations did only occur during moderate or high solar flux years.

This article introduces an empirical model of the occurrence probability of post-sunset F region EPDs called the Ionospheric Bubble Probability (IBP) model. The IBP is derived from the detection of magnetic field perturbations associated with EPDs obtained from 9 years of CHAMP and 8.5 years of Swarm observations in the geomagnetic field. The model predicts the EPD occurrence rate for a given longitude, day of year, local time and solar activity, for the altitude range 350-500 km, and low geographic latitudes of $\pm$ 45°. The occcurrence probability is given in the range of 0 to 1, from a 0% to 100% probability, respectively. The structure of this manuscript goes as following. Section 2 provides a description of the data on which the model is based, section 3 describes the model development methods, section 4 shows the model results, section 5 provides model validation and discussion, and finally, conclusions are described in section 7. The forward model code is available from URL: https://igit.iap-kborn.de/ibp/ibp-model.

2 Data

2.1 Swarm satellite mission

The Swarm satellite mission is a constellation consisting of three identical satellites Alpha, Bravo and Charlie (A, B and C) launched in November 2013 into near-circular orbits at an altitude of approximately 490 km (Friis-Christensen et al., 2006; Olsen et al., 2013). Following orbital maneuvers in April 2014, Swarm A and C fly in a side-by-side configuration with an inclination of 87.4° and an initial altitude of about 460 km (see Figure 1), while Swarm B flies at an inclination of 88° and at a higher orbit of initially about 530 km altitude. Swarm B has been precessing away from the lower pair at a rate of approximately 1.5 h of local time per year while Swarm A and C precess westward in local time at a rate of 2.7 h per month (Knudsen et al., 2017). The Swarm satellites cover all local times about every 4 months. The satellites carry, among other instruments, a magnetometer package consisting of an Absolute Scalar Magnetometer (ASM) and a Vector Field Magnetometer (VSM), which provides precise measurements of the Earth's magnetic field at the satellite location at 1 Hz frequency. Each satellite also carries a spherical Langmuir probe as part of the Electric Field Instrument (EFI) providing plasma density observations at 2 Hz frequency (Knudsen et al., 2017).

It is known that EPDs can be detected by high-precision magnetometers on board low earth orbit (LEO) satellites from their diamagnetic effects as regions of locally depleted plasma are characterized by enhanced magnetic field strength (e.g., Lühr et al., 2003; Stolle et al., 2006; Park et al., 2013). For the Swarm mission, the European Space Agency (ESA) has introduced the Ionospheric Bubble Index (IBI) as a standard Level 2 (L2) data product, which is generated from in situ magnetic field and plasma observations onboard the Swarm satellites and provides detections of EPDs along Swarm orbits. The IBI product considers not only the characteristic small-scale variations in the magnetic field to detect EPDs but also the concurrent change in plasma density to confirm these detected EPDs. The detection threshold of EPDs based on their diamagnetic effects is set to 0.15 nT. If the correlation between the magnetic field and electron density is sufficiently high (i.e. p^2>0.5, where p is the pearson correlation coefficient), which confirms the diamagnetic effect, the magnetic fluctuation is flagged as confirmed EPD. The IBI product provides a binary indicator for each of the low latitude (below 45°), night side (18-06LT), 1 Hz magnetic readings whether the measurement is affected by an EPD or not. If the data quality does not allow for EPD detection, e.g., due to enhanced noise or too many data gaps, the data is flagged by an integer value larger than 1. The detailed description of the IBI product and of its derivation is outlined in Park et al. (2013). Swarm data between 01 January 2014 and 31 December 2022 have been used in this study

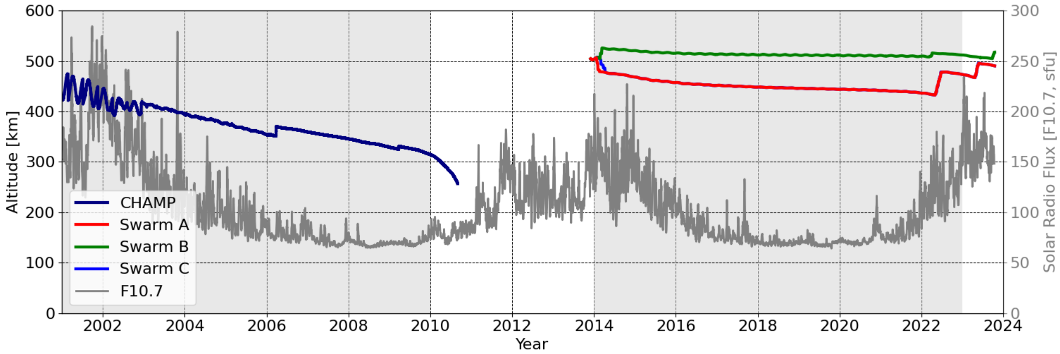

Figure 1. Orbit altitude evolution of the CHAMP and Swarm satellites. The grey line indicates daily values of the F10.7 solar activity index. The light grey areas indicate the times of satellite data which where selected to derive the IBP model.

to derive the model. The mean satellite altitudes were around 480 km for Swarm A and C and 510 km for Swarm B (see Figure 1).

2.2 CHAMP satellite mission

CHAMP (CHallenging Minisatellite Payload) was launched on 15 July 2000 into a near-circular orbit with an inclination of 87.3° and an initial orbit altitude of 456 km (Reigber et al., 2002), which decayed to around 250 km in 2010 when the mission re-entered the atmosphere (see Figure 1). The study of geomagnetic field was one of the objectives behind this satellite mission. CHAMP carried both scalar and vector magnetometers, which provided precise measurements of the Earth's magnetic field at the satellite altitude at 1 Hz frequency. The first global survey of magnetic signatures of EPDs including a description of their detection in the magnetic field was published by Stolle et al. (2006). In order to derive the IBP model, the CHAMP magnetic data was re-processed by the IBI processor as used for the L2 Swarm product to ensure consistency of the detections between Swarm and CHAMP. Since the CHAMP mission provided electron density measurements at only 15 s resolution, the correlation between magnetic field fluctuations and electron density was disabled in the processor when applied to CHAMP, because it was not expected to make meaningful contribution as is the case for the high resolution plasma density data from Swarm. Therefore, all detections in the magnetic field that exceeded a predefined threshold are identified as an EPD. CHAMP data between 01 January 2001 and 31 December 2009 have been used to derive the model. The mean satellite altitude as shown in Figure 1 was around 360 km.

2.3 Comparing CHAMP and Swarm data sets

Figure 2 shows the probability density of orbits with EPD detections over local time for the CHAMP and Swarm satellites for the data periods between 01 January 2001 and 31 December 2022. Figure 2a shows CHAMP data applied to a detection threshold of 0.15 nT for EPDs as implemented for the Swarm IBI processor, but without confirmation through correlation with electron density. In Figure 2c, results for the Swarm satellites are shown under the same conditions as for Figure 2a but the EPDs detected by Swarm A,B,C satellites have been additionally confirmed by correlation with concurrent electron density measurements. In Figure 2c, the probability density of EPDs rapidly increases after 18LT, peaks between 20LT and 22LT and then gradually decreases. Very few EPDs are detected after 02LT. This behaviour is well known from several other independent satellite observations (e.g., Gentile et al., 2006b; Xiong et al., 2010). For the

IBP model, we use the Swarm data that have been processed with a 0.15 nT detection threshold for EPDs and simultaneously correlated with electron density measurements as shown in Figure 2c. The probability density based on CHAMP data with the same threshold of 0.15 nT shows a flatter distribution with a maximum around 22LT and still relatively high values after 02LT in Figure 2a. The relatively large number of EPD detections between 02LT and 06LT for CHAMP, are detections with similar frequency and amplitude to EPDs but do not have corresponding signatures in electron density. Thus, the histogram is smeared out and we obtain a lower local maximum. Figure 2b shows the distribution of EPD detection for CHAMP but with a higher detection threshold of 0.25 nT. This resulting histogram shows reduced detections of EPDs beyond 02LT and a higher probability density between 20-24LT, which is more consistent with observations of EPDs dedections including the correlation between the magnetic field and plasma density. Additionally, when the correlations to electron density is not considered for EPDs detected from Swarm satellites, the probability distribution shown in Figure 2d resembles more closely with the EPD probability distribution shown for CHAMP with 0.25 nT detection threshold in Figure 2b than with the EPD probability distribution for 0.15 nT detection threshold shown in Figure 2a.

For these reasons, the EPD detection thresholds as applied for Figures 2b and 2d have been chosen for CHAMP and Swarm data, respectively, to develop the IBP model. Additionally, we only consider CHAMP and Swarm data during periods with solar flux indices F10.7 $\geq$ 80 s.f.u and during geomagnetic quiet periods with Hp30 indices ≤ 3 (Tapping, 2013; Yamazaki et al., 2022). Setting a threshold for F10.7 improved the performance of the IBP model, e.g., reduces the overestimation of low occurrence rates (see also chapter 5.2).

3 Model development

The IBP model describing the EPD occurrence probability is based on parameter estimations for functions of local time, longitude, day of year (doy) and solar flux level. The model development is based on the assumption that an EPD has a random life-time and that it is detected by the satellite at an arbitrary time during the EPD's existence. We further assume that the time of appearance of an EPD at a certain region has a constant mean and a given variance and may be modeled by a Gaussian distributed random variable. The random lifetime of an EPD is described by an exponential distributed random variable. For each EPD, a realization of its lifetime and its starting time is created which defines its time of existence. In addition, we make use of a Poisson distributed random variable to account for the possibility that several EPDs may appear at the same location during the same night. The parameters of the IBP model are described in Table 1.

We make use of a half orbit integration of the IBI dataset (either ascending or descending), since no latitudinal distribution is modeled and it is also uncertain, if two detections during one pass are in fact the same EPD. If no EPD is detected along the satellite pass, the pass is flagged with 0. If at least one EPB is detected in the subset of IBI data, the pass is flagged with 1. Our model process is thus also constructed to have two

Table 1. The basic model parameters used in the IBP model.

Parameter (units)	Influence	Distribution
$\mu(hours), \sigma(hours)$	mean and variance start-time	Gaussian distribution
λ	plasma bubble intensity	Poisson distribution
$\frac{1}{\gamma}(hours)$	expected lifetime of bubbles	Exponential distribution

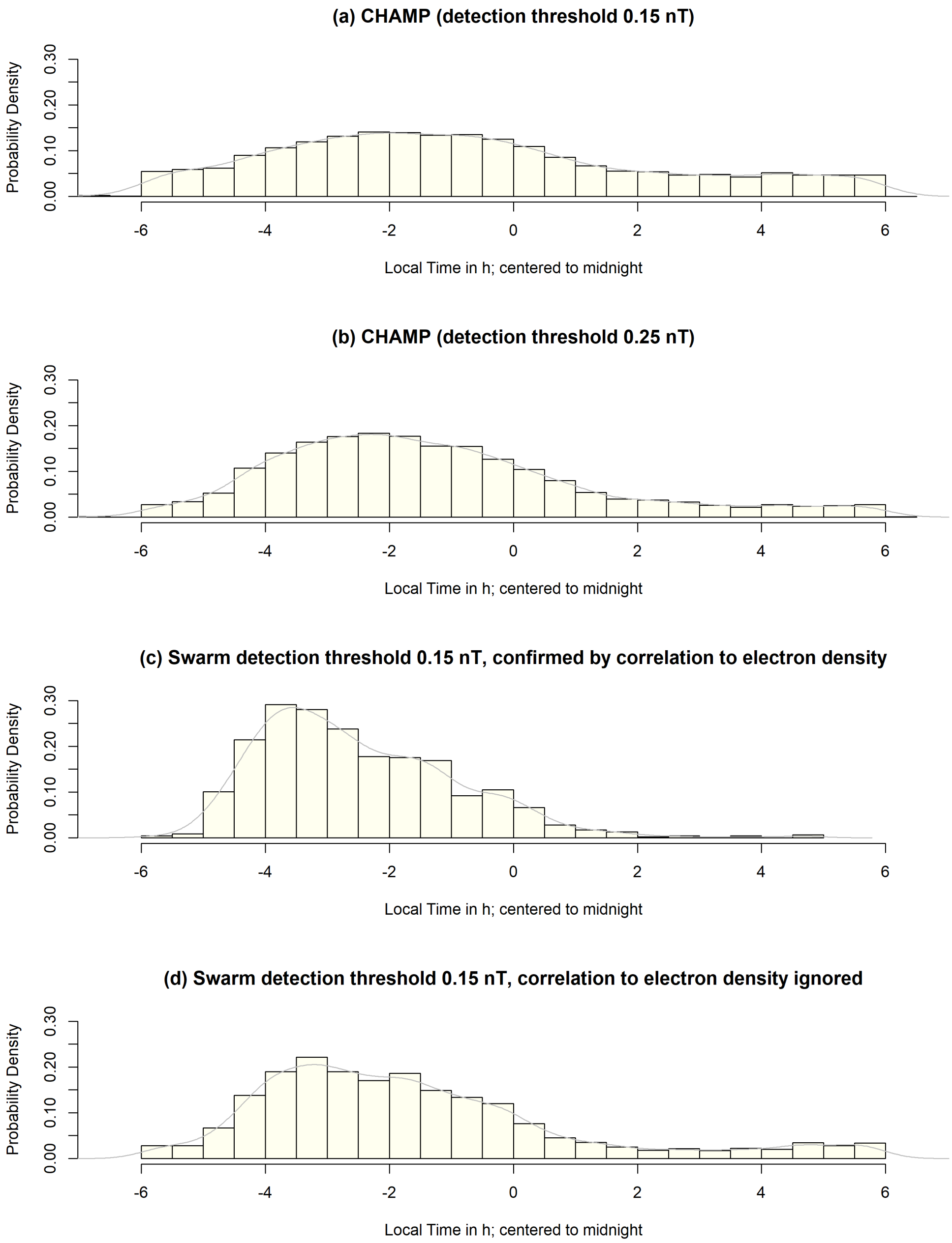

Figure 2. Probability density of orbits with EPD detections over local time for the CHAMP and Swarm missions.

states, 0 and 1. To obtain a state of 1, a minimum one bubble has to appear before the satellite pass and in addition when adding its life time it has to exceed the time of the satellite pass. This may be expressed in the following way. Let $T_0^{(i)}$, $L^{(i)}$, $i \in \mathbb{N}$ be the series of realizations of appearance times (in local time) and lifetimes of EPDs and the number of EPDs in that night be given by n. Then, we can define a process $X(t)$, which describes the state of an EPD being detected during a satellite pass or not. For a given local time, t, we can write:

$$X(t) = \mathbb{1}\left\{ \sum_{i=1}^{n} \mathbb{1}(T_0^{(i)} < t) \cdot \mathbb{1}(T_0^{(i)} + L^{(i)} > t) \right\} \tag{1}$$

The first term of Equation 1 indicates the appearance of the bubble before time, t, while the second term indicates if its end of existence is past t. The function $\mathbb{1}$ represents the indicator function and takes a value of 1 if the condition is valid, else the indicator function is 0. This function represents a process that has two states 0 and 1. A state of 0 denotes that no EPD is detected while a state of 1 denotes that a minimum of one EPD is detected in the satellite pass at the given time, which is identical to the integration of the dataset. Given the distributions (see Table 1), we can rewrite the probability, P, of obtaining a flag of 1 as

$$\begin{aligned} P[X(t) = 1] &= 1 - P[X(t) = 0] \\ &= 1 - P\left[\{ \sum_{i=1}^{N_\lambda} \mathbb{1}(T_0^{(i)} < t) \cdot \mathbb{1}(T_0^{(i)} + L^{(i)} > t) \} = 0 \right] \\ &= 1 - e^{\lambda \cdot I(t,\gamma,\mu,\sigma)} \end{aligned} \tag{2}$$

where the integral $I(t, \gamma, \mu, \sigma)$ is defined as,

$$I(t, \gamma, \mu, \sigma) = \int_{-\infty}^{t} \frac{1}{\sqrt{2\pi}\sigma} e^{(\frac{-(x-\mu)^2}{2\sigma^2})} (-e^{-\gamma(t-x)}) dx \tag{3}$$

The complete derivation of Equation 2 can be found in Appendix A.

3.1 Modeling the bubble intensity parameter

Several parameters of this IBP model are not a single number, but are functions dependent on season, longitude, and F10.7. The global bubble intensity parameter, λ, varies with season, with the F10.7 index and also with longitude and can be represented as,

$$\lambda = \lambda(doy, lon, F10.7) \tag{4}$$

The longitudinal distribution of λ is given by a probability density function $\phi_{month}(lon)$ for each month. Since the integral of a probability density function equals 1, $\phi_{month}(lon)$ is not affecting the global intensity. Thus we may separate into global intensity and longitudinal distribution. The global bubble intensity consists of three parts, a constant (C_1), a linear fit including the F10.7 index ($C_2 \cdot F10.7$) and an estimated function $g_{osc}(doy)$ to describe the seasonal dependency. Eventually λ can be written as

$$\lambda(doy, lon, F10.7) = (g_{osc}(doy) + C_1 + C_2 \cdot F10.7) \cdot \phi_{month}(lon) \tag{5}$$

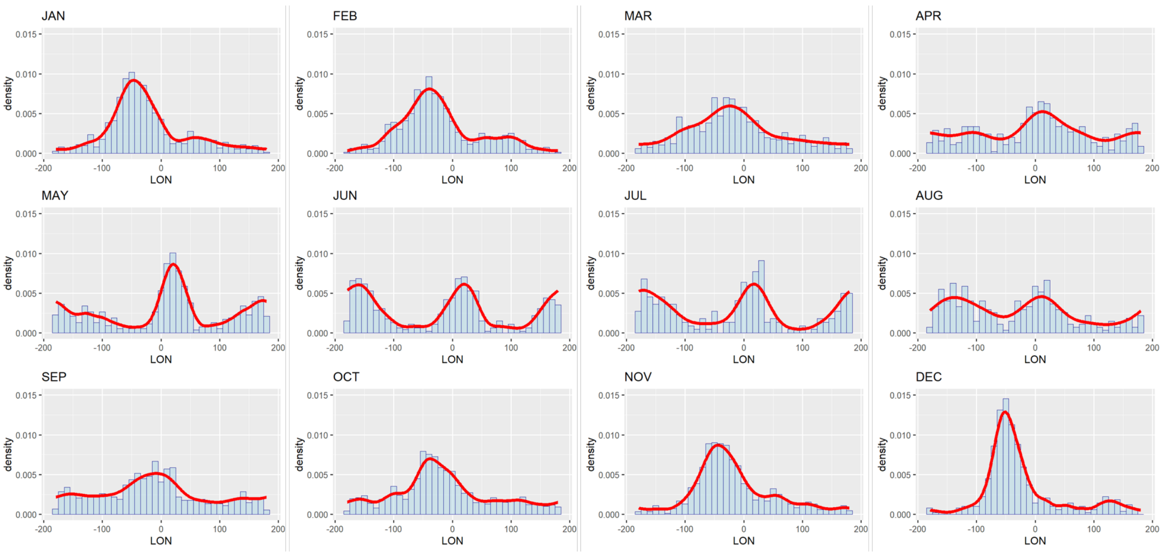

Figure 3. Monthly longitudinal densities obtained using kernel density estimation is shown in solid red lines. The histogram in the background shows the monthly probability density of EPDs as a function of longitude.

By substituting λ in Equation 2, we obtain

$$P[X(t) = 1] = 1 - e^{(g_{osc}(doy)+C_1+C_2\cdot F10.7)\cdot\phi_{month}(lon)\cdot I(t,\gamma,\mu,\sigma)} \tag{6}$$

3.2 Modeling the longitudinal probability density and timeshift functions

The longitudinal probability density function $\phi_{month}(lon)$ is obtained using a kernel density estimation method. The density is estimated from the normalized EPD detections of the CHAMP and Swarm satellites. To determine the optimal bandwidth for the kernel density estimation of $\phi_{month}(lon)$, we apply a direct plug-in method developed by Sheather & Jones (1991). To validate this choice of bandwidth, cross-validation was carried out where the bandwidth selected by employing the Sheather & Jones (1991) method was found to be optimal. We apply this kernel density estimator to the observed bubbles for each month and arrive at the monthly longitudinal densities, which are shown in Figure 3. The solid red lines in this figure show the longitudinal variation of $\phi_{month}(lon)$ for each month. Remarkable, already here, are the higher values of $\phi_{month}(lon)$ over the Atlantic/American sector during the months of November to February and the lower values during May to August. The histogram shown in blue colour gives the monthly probability density of EPDs detected from CHAMP and Swarm satellites as a function of longitude.

The time of appearance of EPD is modeled in this IBP model using a Gaussian distribution with the parameters μ and σ. As it is known that the appearance of EPD may vary with season and longitude (see Figure 8, Stolle et al., 2008), this has been taken into account by adding a monthly timeshift function depending on longitude, $ts_{month}(lon)$, to the parameter μ_0, which can be expressed as

$$\mu(month, lon) = \mu_0 + ts_{month}(lon) \tag{7}$$

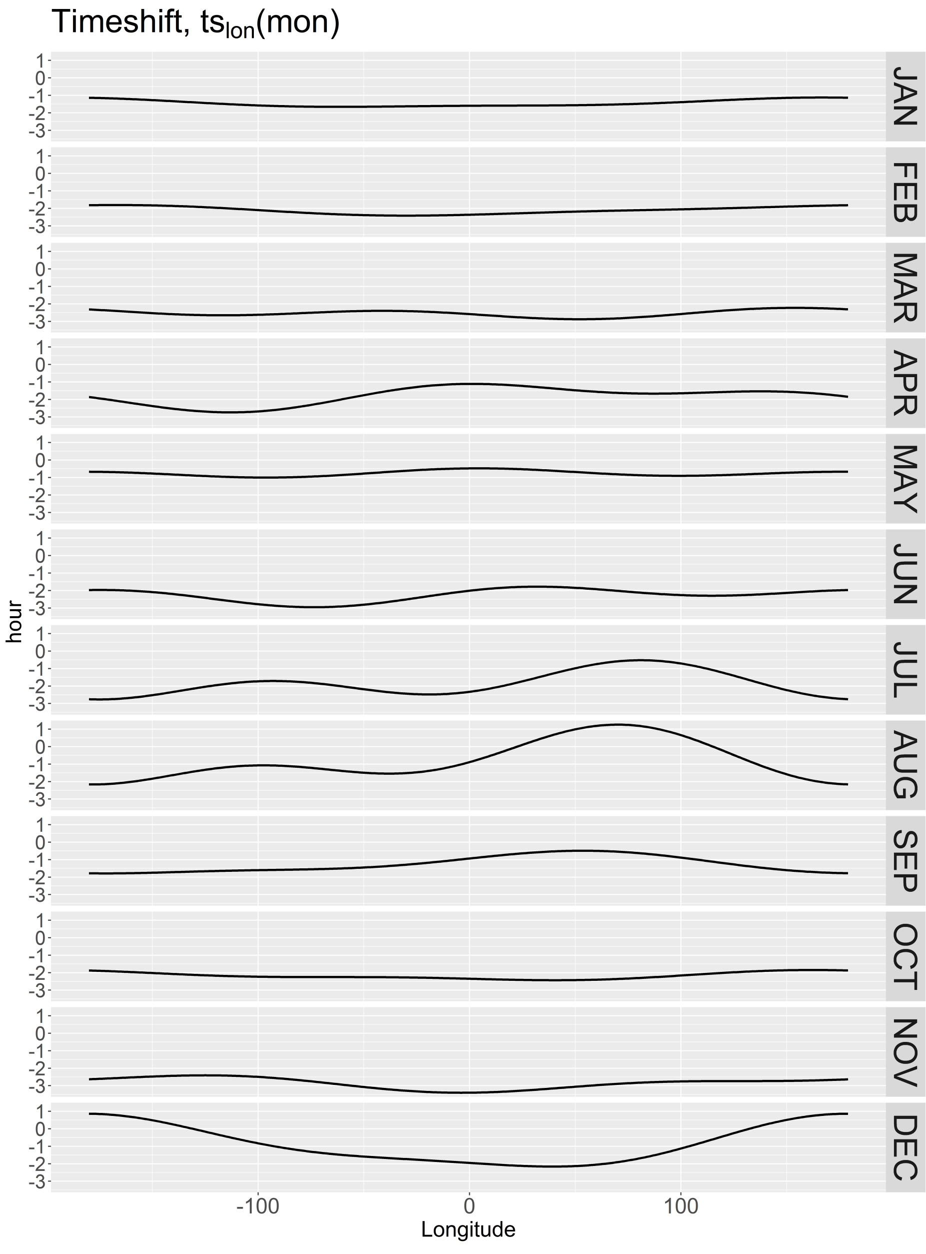

Figure 4. Dependence of monthly timeshift function on longitude. Here in the y-axis, 0 refers to 24 LT.

The monthly variation of $ts_{month}(lon)$ as a function of longitude is shown in Figure 4 where variations of up to 2 hours in $ts_{month}(lon)$ may be observed. The timeshift is estimated using a least-squares fit for the coefficients of the harmonic function described below

$$ts_{month}(lon) = t_0 + \sum_{1}^{2}(t_i^{(s)} sin(i \cdot \frac{lon}{360} \cdot 2\pi)) + (t_i^{(c)} cos(i \cdot \frac{lon}{360} \cdot 2\pi)) \tag{8}$$

The coefficients for the timeshift function can be estimated directly from the local time and the longitude of the detected EPDs using a least-squares fit, since we assume the lifetime parameter γ to be globally constant. However, the constant t_0 may be affected, but this can be compensated by the estimation of parameter μ in a following step. By expanding $I(t, \gamma, \mu, \sigma)$ using Equation 3 and then substituting $ts_{month}(lon)$ in Equation 6, the model takes the following form:

$$\begin{aligned} P[X(t) = 1] = 1 - exp\Bigg\{ & (g_{osc}(doy) + C_1 + C_2 \cdot F10.7) \cdot \phi_{month}(lon) \\ & \cdot \left(\int_{-\infty}^{t} \frac{1}{\sqrt{2\pi}\sigma} exp\left\{ \frac{-(x - (\mu + ts_{month}(lon)))^2}{2\sigma^2} \right\} \left(-e^{-\gamma(t-x)} dx \right) \right\} \end{aligned} \tag{9}$$

Equation 9 provides a probability for each time, t, which is used to estimate whether the current data point is an EPD or not. We compare this estimated probability of EPDs with the observed EPD flag of 0 and 1 in the data and minimize the root mean square error (RMSE) to estimate the parameters $\mu, \sigma, \gamma, C1$ and $C2$. It is important to note that since $g_{osc}(doy)$ is determined at a later step, we use λ_{tmp} in place of λ by setting $g_{osc}(doy)$ to 0 in Equation 9 while estimating $\mu, \sigma, \gamma, C1$ and $C2$, where λ_{tmp} is given by

$$\lambda_{tmp} = (C_1 + C_2 \cdot F10.7) \cdot \phi_{month}(lon) \tag{10}$$

and

$$RMSE = \sqrt{\frac{1}{n}\sum_{i=1}^{n}(Flag_i - P_i)^2} \tag{11}$$

This RMSE was minimized using a BFGS (Broyden-Fletcher-Goldfarb-Shanno) method. This minimization method also has the option of passing on boundary conditions. To ensure that the actual minimum was reached reliably, the minimization was performed multiple times with randomized starting points.

After estimating $\mu, \sigma, \gamma, C1$ and $C2$ using Equation 9, we now estimate $g_{osc}(doy)$, which is a periodic function that takes the seasonal variability of the intensity of the EPDs into account. Without including this parameter in λ, the model cannot account for the well-known seasonal variability of EPDs. To resolve this issue, the residuals between the number of EPDs that are observed in the data and the number that are estimated by the model over a 5-day moving period are computed. From these residuals, a least-squares fit to estimate the coefficients for $g_{osc}(doy)$ is performed. The function $g_{osc}(doy)$ is developed using a harmonic expansion and reads as

$$g_{osc}(doy) = g_0 + \sum_{1}^{2}(g_i^{(s)} sin(i \cdot \frac{doy}{365} \cdot 2\pi)) + (g_i^{(c)} cos(i \cdot \frac{doy}{365} \cdot 2\pi)) \tag{12}$$

Table 2. IBP model coefficients

$C1$	$C2$	$\frac{1}{\gamma}$ (hours)	μ (hours)	σ (hours)
-221.7870	4.3522	1.4121	-1.3386	1.0754

In summary, the procedure for solving for the parameters and coefficients of the IBP model follows the following steps:

1. estimate monthly time-shift coefficients
2. estimate monthly longitudinal densities
3. estimate the global coefficients $\mu, \sigma, \gamma, C1$ and $C2$
4. compute residuals and estimate the coefficients for g_{osc}

The values of the coefficients $\mu, \sigma, \gamma, C1$ and $C2$ obtained after minimization are summarized in Table 2.

4 Results

4.1 Climatology of EPD occurrence derived by the IBP model

We first evaluate the IBP model with a constant input value of F10.7=150 s.f.u to examine if it is capable of describing the seasonal, longitudinal and localtime distributions of EPDs that has been discussed in earlier works based on CHAMP, Swarm and other LEO satellite missions (e.g., Stolle et al., 2006; Gentile et al., 2006b; Xiong et al., 2010; Aa et al., 2020). The longitudinal and temporal distribution of EPDs along with its occurrence probability are shown in Figure 5 for solstice (June and December) and equinox months (March and September). The IBP model reproduces high occurrence probability of EPDs ranging between 50-90% over the South-American sector (75-25°W) and low occurrence probability over the Pacific sector (180-120°W) during the December solstice. For this period, EPDs over the South American sector arise around 20 LT, peak between 21 and 22 LT and then rapidly decrease after 23 LT, which is consistent with its climatological variations as reported by the earlier independent works cited above. For the March/September equinox months, high occurrence probability of EPDs ranging between 50-70% is seen to extend eastward from the South American sector over to the West African sector (75°W-30°E). The temporal variation of EPDs for these periods differ slightly as the occurrence probability of EPDs peaks around 21 LT during March and an hour later, around 22 LT, during September. Significant EPDs occurrence probability reaching about 40% is also seen over the Pacific sector during equinox months. The IBP model records high occurrence probability of EPDs during June over the African (25°W-50°E) and Pacific sectors in pre-midnight hours while minima is recorded over the South American sector.

4.2 Dependence of EPD occurrence on solar activity

The occurrence of EPDs shows an evident dependence on solar activity with EPDs being more prevalent under solar maximum than solar minimum conditions (e.g., Gentile et al., 2006a). The performance of the IBP model in simulating the variability of EPDs under varying solar flux conditions is given in Figure 6. On the basis of the F10.7 index, we assess whether the IBP model reproduces a more frequent occurrence of EPDs under solar maximum than solar minimum conditions. We present the monthly global occurrence rate of EPDs derived from the IBP model with F10.7 index ranging between 80 and 200 s.f.u with increasing steps of 40 s.f.u in Figure 6. The monthly global occur-

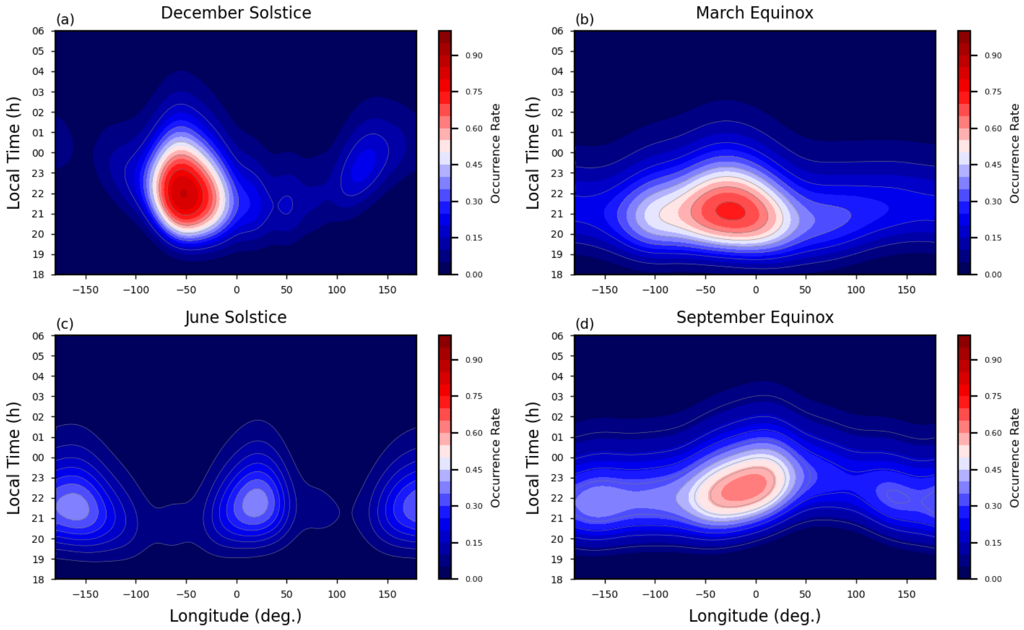

Figure 5. Occurrence probability of EPDs presented as a function of longitude and local time predicted by the IBP model at a constant F10.7 index of 150 s.f.u during (a) December, (b) March, (c) June, and (d) September.

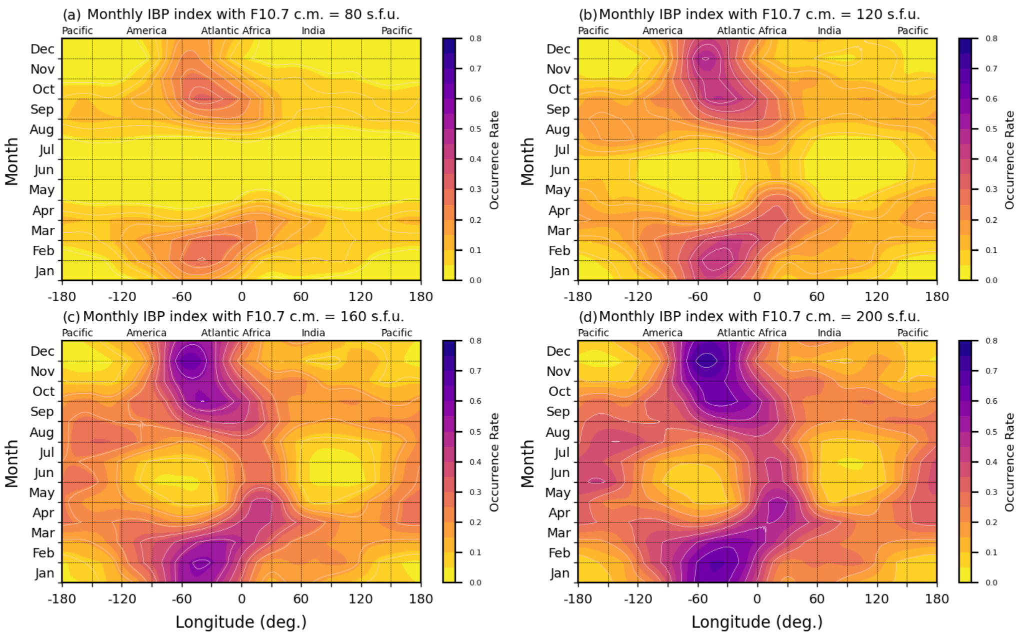

Figure 6. Occurrence probability of EPDs presented as a function of longitude and month predicted by the IBP model at F10.7 values of (a) 80 s.f.u, (b) 120 s.f.u, (c) 160 s.f.u and (d) 200 s.f.u.

rence rate from the IBP model, referred henceforth as monthly IBP index, is derived for a fixed value of F10.7 for all integer longitudes at a resolution of 5° at the middle of each month and averaged between 19 and 01 LT. We find that the IBP model reproduces the expected positive linear relationship between EPD occurrence rates and F10.7 index. The monthly IBP index generally retains negligible probabilities for F10.7 at 80 s.f.u except in the America-Atlantic-Africa sector during the equinoxes and solstice periods. However, with increasing F10.7 levels, the monthly IBP indices begin to show significant probabilities as EPDs become more prevalent. Besides, with F10.7 at 120 s.f.u and above, the seasonal and longitudinal variations of the EPD occurrence rates are particularly well-characterized by the IBP model compared to its climatology (e.g., Gentile et al., 2006a) with monthly IBP index reaching highest rates around the equinoxes and winter solstice in the America-Atlantic-Africa region and lowest rates during November-February in the Pacific sector and during May-July in the America-Atlantic and Indian sectors. The results from the IBP model showing a dependence on F10.7 levels compares well with the findings of Gentile et al. (2006b), which showed the climatology of EPD based on 15 years of plasma density measurements using the Defense Meteorological Satellite Program (DMSP) satellites.

5 Assessment of the IBP model

5.1 Overview of assessment methods

The performance of probabilistic predictions by models developed for space weather phenomena have been typically quantified in the literature using skill scores and relative (receiver) operating characteristic (ROC) curves (e.g., Barnes et al., 2016; Murray et al., 2017; Nishizuka et al., 2020). A skill score is generally defined as the measure of accuracy of forecasts of interest relative to the accuracy of the forecasts produced by some reference procedure (Murphy, 1988). A generic skill score takes the following form,

$$Skill\ Score = \frac{A_{forecast} - A_{reference}}{A_{perfect} - A_{reference}} \tag{13}$$

where $A_{forecast}$ is the accuracy of the forecasting method under consideration, $A_{perfect}$ is the accuracy of a perfect forecast and $A_{reference}$ is the accuracy of a reference method or the accuracy that is attainable by chance, which is usually chosen to be the climatology of the considered event. For probabilistic forecasts, a measure of accuracy is the mean square error (MSE), which can be used to calculate $A_{forecast}$ as shown in Barnes et al. (2016) in the following way,

$$A_{forecast} = MSE(p_f, o) = \langle (p_f - o)^2 \rangle \tag{14}$$

where p_f is the forecast probability from the considered method and o is the value for binary outcomes ($o = 0$ for non event, $o = 1$ for an event). The MSE for a perfect forecast, $A_{perfect}$, is 0.

In this work, we use the Brier Skill Score (BSS) (Wilks, 1995) for evaluating the probability forecasting capability of the IBP model. BSS is calculated from the Brier score (BS) and climatological Brier score (BS_c) by using the following equation,

$$BSS = \frac{BS - BS_c}{0 - BS_c} \tag{15}$$

where $BS = MSE(p_f, o)$ and $BS_c = MSE(\langle o \rangle, o)$. BSS can be complemented by a reliability diagram, which compares the forecast probabilities with the observed frequency of the events.

The quality of the probability forecasts are also assessed by using the ROC curve, which relates the true positive rate (TPR) or the probability of detection (POD) against the corresponding false alarm rate (FAR) (e.g., Swets, 1973; Mason, 1982). TPR or POD and FAR can be easily understood in case of a binary categorical forecasting system using a 2×2 contingency table (see Table 3).

Table 3. 2×2 contingency table for a binary, categorical forecasting system

	Forecasts		
Observation	Positive	Negative	Total
Event	True Positive (TP)	False Negative (FN)	TP+FN
Nonevent	False Positive (FP)	True Negative (TN)	FP+TN
Total	TP+FP	FN+TN	N=TP+FP+FN+TN

From the contingency table, POD and FAR are defined as follows (e.g., Mason, 1982)

$$POD = \frac{TP}{TP + FN} \quad and \quad FAR = \frac{FP}{FP + TN} \tag{16}$$

Probabilistic forecasts can be converted to binary, categorical forecasts by selecting a probability threshold, P_{th}, such that any forecast probability over the threshold is considered to be a forecast for an event, and anything less is considered to be a forecast for a non-event. By varying this threshold value, contingency tables along with corresponding POD and FAR can be determined for every P_{th} and based on these resulting POD and FAR values, a ROC curve can be obtained. As POD and FAR are the axes of the ROC curve and they range between 0 and 1, the ROC curve for no-skill forecasts coincides with the 45° line from the origin passing through (0,0) and (1,1) with POD and FAR being equal. For a perfect forecast, the ROC curve connects the points (0,0), (0,1) and (1,1) with the values of POD and FAR being 1 and 0, respectively. The accuracy of binary, categorical forecasts can be determined using standard skill scores and can be summarized by the ROC Skill Score (ROCSS), also known as the Gini coefficient G1 (e.g., Jolliffe & Stephenson, 2012) and by the Hanssen and Kuiper's Discriminant (H&KSS), also known as the true skill statistic (TSS) or the Peirce skill score (e.g., Hanssen & Kuipers, 1965; Murhy, 1993). $G1 = 2 \times A - 1.0$ where A is the area under the ROC curve, and G1 = 1.0 denotes a perfect score. H&KSS can be written as,

$$H\&KSS = POD - FAR \tag{17}$$

H&KSS takes into account the success due to random guessing and it ranges between -1 and +1. A score of +1 indicates perfect agreement between predictions and observations while a score of 0 or less indicate no-skill forecasting capability. As H&KSS can be sensitive to P_{th}, we also calculate the Gini coefficient to present a concise summary of the assessment of the IBP model.

5.2 Model evaluation

We use one year of recent IBI index data from the Swarm A, B and C satellites between July 2022 and June 2023 for the purpose of IBP model validation. During this period, the total number of orbits with and without EPD for each Swarm satellite are summarized in Table 4. For each orbit of the satellite, we first compute the EPD occurrence probability from the IBP model for all longitude and local time that the satellite traverses. These probability outputs are then used to derive the maximum EPD occurrence probability for each satellite orbit. With different choices of probability threshold, P_{th}, we predict using this derived maximum EPD occurrence probability whether each satellite orbit contains or not contains EPD. The contingency tables for binary, categorical forecasts of EPD is then created by varying P_{th} and compared with the observed IBI data set. We chose a threshold step of 0.02 resulting in covering the P_{th} levels between 0 and 1. Thereafter, POD and FAR values are calculated for different contingency tables and ROC curves are generated for Swarm A, B and C satellites. These ROC curves are presented in the upper panels of Figure 7 and are used to visualize H&KSS. When P_{th} is set to 1, no EPD detections are forecasted and hence TP=FP=0, which corresponds to the point (0,0) on the ROC curves. When P_{th} is set to 0, all detections are forecasted as EPD and hence FN=TN=0, which corresponds to the point (1,1) on the ROC curves. For Figures 7a-7c, we find that ROC curves stay well above the 45° no-skill forecast line shown here in dashed green color. The ROC curves also stay close to the FAR=0 while the POD rises, which suggests that the IBP model well forecasts EPD events. For Swarm satellites A, B and C, we find that H&KSS maximizes at at similar values, e.g., when P_{th} equals 0.22, 0.18 and 0.18, respectively, which is shown through dashed vertical black lines. H&KSS values reach 0.66, 0.73 and 0.65 for satellites A, B and C, respectively, which suggests that the forecasting capability of the IBP model is significantly better than a no-skill forecast. The Gini coefficient for Swarm A, B and C satellites are 0.80, 0.86 and 0.80, respectively.

Table 4. Total number of orbits with and without EPD for each Swarm satellite between July 2022 and June 2023

Satellite	# of orbits		
	Total	with EPDs	without EPDs
A	3165	334	2831
B	3294	262	3032
C	3189	357	2832

In the lower panels of Figure 7, the BSS score and reliability plots that accompany it are presented for the three Swarm satellites. The BSS for Swarm A, B and C equal 0.317, 0.320 and 0.316, respectively. The reliability plots are constructed by first selecting probability intervals and then the frequency of observed events within each interval is estimated using the method described in Wheatland (2005). This observed frequency is then plotted against the predicted probability and the error bars are estimated based on the number of events that lie within each interval. On a reliability plot, perfect prediction corresponds to a 45° line when observed frequency equals the predicted probability, which is plotted here using the dashed green lines in Figure 7d-f. Points lying above this line indicate underprediction while points located below this line imply overprediction. We find that the IBP model underestimates the occurrence frequency of EPD when the predicted probability exceeds 0.7 for all three satellites. Below this predicted probability value, the model slightly overestimates the occurrence frequency of EPD for all three satellites. We found, that the overestimation for low occurrence rates increases with the amount of data of very low solar flux. These times are usually free of EPD detections in the topside F region. A reasonable results as shown in Figure 7, was found for a cutoff of F10.7 $\leq$ 80 s.f.u.. In summary, the model slightly underestimates the EPD occurrence at occasions of high EPD probability and it slightly overestimates the EPD occurrence of low EPD probability. The performance of the IBP model based on the evaluation metrics used here above is summarized in Table 5.

Table 5. IBP model performance based on the evaluation metrics for Swarm data between July 2022 and June 2023

Satellite	H&KSS (P_{th})	G1	BSS
A	0.66 (0.22)	0.80	0.317
B	0.73 (0.18)	0.86	0.320
C	0.65 (0.18)	0.80	0.316

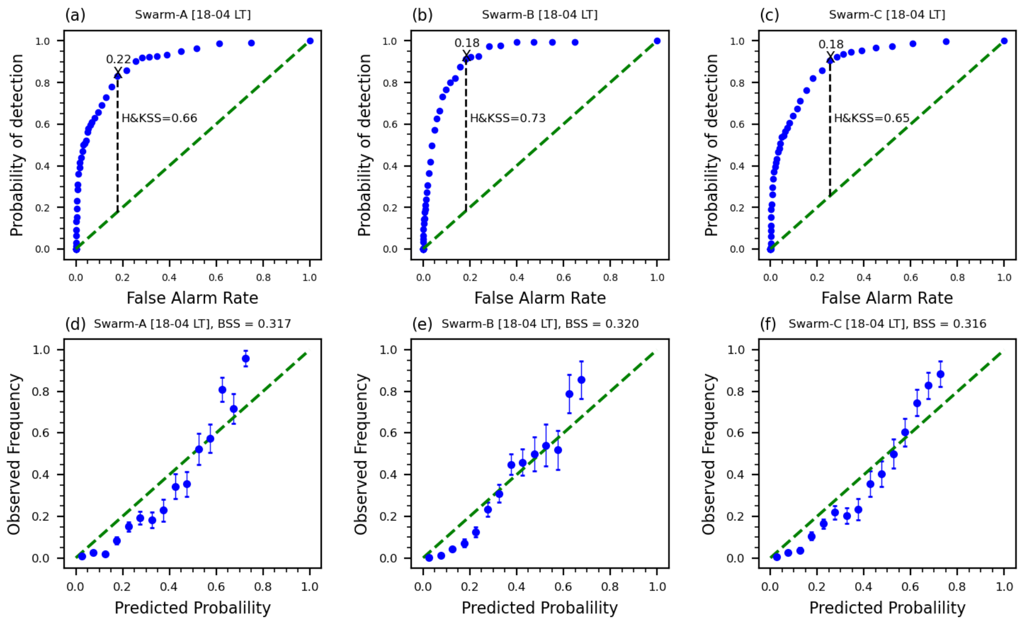

Figure 7. The top panels of the figure (a-c) show receiver operating characteristic (ROC) plots depicting the probability of detection as a function of the false alarm rate by varying the threshold above which an EPD is forecasted. In this case the maximum H&KSS occurs for p = 0.22, 0.18, 0.18 for Swarm A, B and C, respectively and is indicated by a dashed vertical line. The random classifier line of the ROC plots is donated in dashed green colors. The bottom panels (d-f) show reliability plots in which the observed frequency of EPDs is plotted as a function of the forecast probability. Perfect reliability occurs when all points lie on the diagonal (x=y) line. The error bars are based on the sample sizes in each relevant bin.

6 Application of the IBP model

The IBP model estimates the occurrence probability of post-sunset equatorial plasma irregularities between 0 (EPDs not at all expected to occur) and 1 (EPDs are fully expected to occur) for a given longitude, local time, day of year, and solar flux value. The performance of the IBP model has been assessed as an estimate largely exceeding a non-skilled forecast in section 5. Thus, the model can be used to predict IBP ocurrence with reasonable confidence. The model forward code is publicly made available, as being an official L2 product of the Swarm mission as given at `https://swarmhandbook.earth.esa.int/catalogue/SW_IBP_CLI_2_`. The forward model code itself and its documentations are available at Gitlab via `https://igit.iap-kborn.de/ibp/ibp-model`. The model code is provided in Python and is also available as a Python package. The model coefficients will be updated with time, when more Swarm observations will be available. A yearly update is anticipated. Updates will be declared in the Gitlab documentation.

Besides the consideration of the assessment results given in section 5, the user of the IBP model shall be aware of the following constraints. The IBP model

- estimates the EPD occurrence rate at altitudes between 350 and 500 km, and does not give information on EPDs which do not reach these altitudes.
- is not recommended to be applied for solar flux indices F10.7 $\leq$ 80 s.f.u. and F10.7 $\geq$ 200 s.f.u..
- does not predict EPD occurrence depending on latitude. It provides the EPD occurrence for a user-defined longitude, but integrated over latitude.

7 Conclusions

In this study, we have presented the IBP model by explaining its derivation, its assessment, and giving recommendations for its application. The main findings of this study are summarized below:

- The IBP model is a statistical climatological model for predicting the occurrence probability of F region EPDs for a given local time, solar radio flux, day of year, and longitude.
- It fully captures the climatology and solar flux dependence of EPDs at altitudes between 350 and 500 km. The model especially performs well in the American/Atlantic sector during December solstice and increased solar activity conditions, which is encouraging as this region and this season is a hotspot for EPDs.
- Based on one year of recent Swarm magnetic data, which constitutes as partly non-trained data set for the assessment, the IBP model has been evaluated and various evaluation metrics have been presented. The IBP model shows improved prediction capability compared to climatological forecasts with moderate skill scores. With the addition of more recent Swarm data, e.g., by updating the model parameters, it is expected that the skill scores and accuracy of the IBP model enhances further.
- The IBP model is publicly made available at `https://igit.iap-kborn.de/ibp/ibp-model`.

8 Open Research

The CHAMP magnetic data set used in this paper (Rother & Michaelis, 2019) can be freely downloaded using the following ftp link, `ftp://anonymous@isdcftp.gfz-potsdam.de/champ/`. How to access the data and data citations can be found under `https://isdc.gfz-potsdam.de/champ-isdc/access-to-the-champ-data/`. The Swarm data set is publicly available from the European Space Agency website using the following website link `https://earth.esa.int/eogateway/missions/swarm/data`. The IBP model is publicly available with the Gitlab link `https://igit.iap-kborn.de/ibp/ibp-model`. The F10.7 index is accessible at `https://lasp.colorado.edu/lisird/data/noaa_radio_flux`. The Hp30 index (Matzka et al., 2022) is provided at `https://kp.gfz-potsdam.de/en/hp30-hp60`. All data sets and software are freely available from the stated links without the need for user registration. The CHAMP magnetic data set and the Hp30 index are published under licence CC BY 4.0.

Acknowledgments

This work has been partly supported by Swarm DISC activities funded by ESA under contract no. 4000109587/13/I-NB.

Appendix A Derivation of Equation 2

$$\begin{aligned}
P[X(t)=1] &= 1 - P[X(t)=0] \\
&= 1 - P\left[\{\sum_{i=1}^{N_\lambda} \mathbb{1}(T_0^{(i)} < t)\cdot \mathbb{1}(T_0^{(i)} + L^{(i)} > t)\} = 0\right] \\
&= 1 - \sum_{i=1}^{\infty} e^{-\lambda}\frac{\lambda^k}{k!} P\left[\mathbb{1}(T_0^{(1)} < t)\cdot \mathbb{1}(T_0^{(1)} + L^{(1)} > t) = 0\right]^i \\
&= 1 - \sum_{i=1}^{\infty} e^{-\lambda}\frac{\lambda^k}{k!} (1 - P\left[\mathbb{1}(T_0^{(1)} < t)\cdot \mathbb{1}(T_0^{(1)} + L^{(1)} > t) = 1\right])^i \\
&= 1 - \sum_{i=1}^{\infty} e^{-\lambda}\frac{\lambda^k}{k!} (P\left[T_0^{(1)} > t\right] + P\left[T_0^{(1)} + L^{(1)} < t\right])^i \\
&= 1 - e^{-\lambda}\cdot e^{\lambda\cdot(P\left[T_0^{(1)} > t\right] + P\left[T_0^{(1)} + L^{(1)} < t\right])} \\
&= 1 - e^{\lambda\cdot(P\left[T_0^{(1)} > t\right] + P\left[T_0^{(1)} + L^{(1)} < t\right] - 1)} \\
&= 1 - e^{\lambda\cdot(-P\left[T_0^{(1)} < t\right] + P\left[T_0^{(1)} + L^{(1)} < t\right])} \\
&= 1 - e^{\lambda\cdot(-\int_{-\infty}^{t} \frac{1}{\sqrt{2\pi}\sigma} e^{(\frac{-(x-\mu)^2}{2\sigma^2})} dx + \int_{-\infty}^{t} \frac{1}{\sqrt{2\pi}\sigma} e^{(\frac{-(x-\mu)^2}{2\sigma^2})} P\left[L^1 < t-x\right] dx} \\
&= 1 - e^{\lambda\cdot(-\int_{-\infty}^{t} \frac{1}{\sqrt{2\pi}\sigma} e^{(\frac{-(x-\mu)^2}{2\sigma^2})} dx + \int_{-\infty}^{t} \frac{1}{\sqrt{2\pi}\sigma} e^{(\frac{-(x-\mu)^2}{2\sigma^2})} (1 - e^{-\gamma\cdot(t-x)}) dx} \\
&= 1 - e^{\lambda\cdot\left(\int_{-\infty}^{t} \frac{1}{\sqrt{2\pi}\sigma} e^{(\frac{-(x-\mu)^2}{2\sigma^2})} (-e^{-\gamma(t-x)}) dx\right)} \\
&= 1 - e^{\lambda\cdot I(t,\gamma,\mu,\sigma)}
\end{aligned} \tag{A1}$$

References

Aa, E., Zhang, S.-R., Coster, A. J., Erickson, P. J., & Rideout, W. (2023). Multi-instrumental analysis of the day-to-day variability of equatorial plasma bubbles. *Frontiers in Astronomy and Space Sciences*, *10*. doi: https://doi.org/10.3389/fspas.2023.1167245

Aa, E., Zou, S., & Liu, S. (2020). Statistical Analysis of Equatorial Plasma Irregularities Retrieved From Swarm 2013–2019 Observations. *Journal of Geophysical Research: Space Physics*, *125*(4), e2019JA027022. doi: https://doi.org/10.1029/2019JA027022

Abdu, M. A. (2019). Day-to-day and short-term variabilities in the equatorial plasma bubble/spread F irregularity seeding and development. *Progress in Earth and Planetary Science*, *6*(1), 11. doi: https://doi.org/10.1186/s40645-019-0258-1

Abdu, M. A., de Medeiros, R. T., Bittencourt, J. A., & Batista, I. S. (1983). Vertical ionization drift velocities and range type spread F in the evening equatorial ionosphere. *Journal of Geophysical Research: Space Physics*, *88*(A1), 399-402. doi: https://doi.org/10.1029/JA088iA01p00399

Balsley, B. B., Haerendel, G., & Greenwald, R. A. (1972). Equatorial spread F: Recent observations and a new interpretation. *Journal of Geophysical Research (1896-1977)*, *77*(28), 5625-5628. doi: https://doi.org/10.1029/JA077i028p05625

Barnes, G., Leka, K. D., Schrijver, C. J., Colak, T., Qahwaji, R., Ashamari, O. W., ... Wagner, E. L. (2016). A comparison of flare forecasting methods. I. Results from the "All-Clear" workshop. *The Astrophysical Journal*, *829*(2), 89. doi: https://10.3847/0004-637X/829/2/89

Basu, S., Basu, S., Huba, J., Krall, J., McDonald, S. E., Makela, J. J., ... Groves, K. (2009). Day-to-day variability of the equatorial ionization anomaly and scintillations at dusk observed by GUVI and modeling by SAMI3. *Journal of Geophysical Research: Space Physics*, *114*(A4). doi: https://doi.org/10.1029/2008JA013899

Burke, W. J., Gentile, L. C., Huang, C. Y., Valladares, C. E., & Su, S. Y. (2004). Longitudinal variability of equatorial plasma bubbles observed by DMSP and ROCSAT-1. *Journal of Geophysical Research: Space Physics*, *109*(A12). doi: https://doi.org/10.1029/2004JA010583

Carter, B. A., Yizengaw, E., Retterer, J. M., Francis, M., Terkildsen, M., Marshall, R., … Zhang, K. (2014). An analysis of the quiet time day-to-day variability in the formation of postsunset equatorial plasma bubbles in the Southeast Asian region. *Journal of Geophysical Research: Space Physics*, *119*(4), 3206-3223. doi: https://doi.org/10.1002/2013JA019570

Chou, M.-Y., Pedatella, N. M., Wu, Q., Huba, J. D., Lin, C. C. H., Schreiner, W. S., … Yue, J. (2020). Observation and Simulation of the Development of Equatorial Plasma Bubbles: Post-Sunset Rise or Upwelling Growth? *Journal of Geophysical Research: Space Physics*, *125*(12), e2020JA028544. doi: https://doi.org/10.1029/2020JA028544

Clemesha, B., & Wright, R. (1966). Spread-F and its Effects upon Radio Wave Propagation and Communications. *P. Newman, Têchnivision. England*, 3.

Dabas, R. S., Singh, L., Lakshmi, D. R., Subramanyam, P., Chopra, P., & Garg, S. C. (2003). Evolution and dynamics of equatorial plasma bubbles: Relationships to ExB drift, postsunset total electron content enhancements, and equatorial electrojet strength. *Radio Science*, *38*(4). doi: https://doi.org/10.1029/2001RS002586

Das, S. K., Patra, A. K., & Niranjan, K. (2021). On the Assessment of Day-To-Day Occurrence of Equatorial Plasma Bubble. *Journal of Geophysical Research: Space Physics*, *126*(5), e2021JA029129. doi: https://doi.org/10.1029/2021JA029129

Fagundes, P. R., Sahai, Y., Batista, I. S., Abdu, M. A., Bittencourt, J. A., & Takahashi, H. (1999). Observations of day-to-day variability in precursor signatures to equatorial F-region plasma depletions. *Annales Geophysicae*, *17*(8), 1053–1063. doi: https://10.1007/s00585-999-1053-x

Farley, D. T., Balsey, B. B., Woodman, R. F., & McClure, J. P. (1970). Equatorial spread F: Implications of VHF radar observations. *Journal of Geophysical Research (1896-1977)*, *75*(34), 7199-7216. doi: https://doi.org/10.1029/JA075i034p07199

Fejer, B. G., Scherliess, L., & de Paula, E. R. (1999). Effects of the vertical plasma drift velocity on the generation and evolution of equatorial spread F. *Journal of Geophysical Research: Space Physics*, *104*(A9), 19859-19869. doi: https://doi.org/10.1029/1999JA900271

Friis-Christensen, E., Lühr, H., & Hulot, G. (2006). Swarm: A constellation to study the Earth's magnetic field. *Earth, Planets and Space*, *58*(4), 351-358. doi: https://doi.org/10.1186/BF03351933

Fukao, S., Yokoyama, T., Tayama, T., Yamamoto, M., Maruyama, T., & Saito, S. (2006). Eastward traverse of equatorial plasma plumes observed with the Equatorial Atmosphere Radar in Indonesia. *Annales Geophysicae*, *24*(5), 1411–1418. Retrieved from `https://angeo.copernicus.org/articles/24/1411/2006/` doi: 10.5194/angeo-24-1411-2006

Gentile, L. C., Burke, W. J., & Rich, F. J. (2006a). A climatology of equatorial plasma bubbles from DMSP 1989–2004. *Radio Science*, *41*(5). doi: https://doi.org/10.1029/2005RS003340

Gentile, L. C., Burke, W. J., & Rich, F. J. (2006b). A global climatology for equatorial plasma bubbles in the topside ionosphere. *Annales Geophysicae*, *24*(1), 163–172. doi: https://doi.org/10.5194/angeo-24-163-2006

Gentile, L. C., Burke, W. J., Roddy, P. A., Retterer, J. M., & Tsunoda, R. T.

(2011). Climatology of plasma density depletions observed by DMSP in the dawn sector. *Journal of Geophysical Research: Space Physics*, *116*(A3). doi: https://doi.org/10.1029/2010JA016176

Haerendel, G. (1973). Theory of equatorial spread F. *Space Plasma Physics of Near-Earth Environment, MPI for Extraterrestrial Physics, Max Planck Society*.

Hanssen, A., & Kuipers, W. (1965). *On the relationship between the frequency of rain and various meteorological parameters. (With reference to the problem of objective forecasting)*. Koninklijk Nederlands Meteorologisch Instituut.

Huang, C.-S., de La Beaujardiere, O., Roddy, P. A., Hunton, D. E., Liu, J. Y., & Chen, S. P. (2014). Occurrence probability and amplitude of equatorial ionospheric irregularities associated with plasma bubbles during low and moderate solar activities (2008–2012). *Journal of Geophysical Research: Space Physics*, *119*(2), 1186-1199. doi: https://doi.org/10.1002/2013JA019212

Huang, C.-S., & Hairston, M. R. (2015). The postsunset vertical plasma drift and its effects on the generation of equatorial plasma bubbles observed by the C/NOFS satellite. *Journal of Geophysical Research: Space Physics*, *120*(3), 2263-2275. doi: https://doi.org/10.1002/2014JA020735

Hysell, D., & Burcham, J. (2002). Long term studies of equatorial spread F using the JULIA radar at Jicamarca. *Journal of Atmospheric and Solar-Terrestrial Physics*, *64*(12), 1531-1543. (Equatorial Aeronomy) doi: https://doi.org/10.1016/S1364-6826(02)00091-3

Hysell, D. L., Fang, T. W., & Fuller-Rowell, T. J. (2022). Modeling equatorial f-region ionospheric instability using a regional ionospheric irregularity model and wam-ipe. *Journal of Geophysical Research: Space Physics*, *127*(9), e2022JA030513. doi: https://doi.org/10.1029/2022JA030513

Hysell, D. L., Rojas, E., Goldberg, H., Milla, M. A., Kuyeng, K., Valdez, A., ... Bourne, H. (2021). Mapping irregularities in the postsunset equatorial ionosphere with an expanded network of hf beacons. *Journal of Geophysical Research: Space Physics*, *126*(7), e2021JA029229. doi: https://doi.org/10.1029/2021JA029229

Hysell, D. L., & Seyler, C. E. (1998). A renormalization group approach to estimation of anomalous diffusion in the unstable equatorial F region. *Journal of Geophysical Research: Space Physics*, *103*(A11), 26731-26737. doi: https://doi.org/10.1029/98JA02616

Jolliffe, I. T., & Stephenson, D. B. (2012). *Forecast verification: a practitioner's guide in atmospheric science*. John Wiley & Sons.

Kelley, M. C. (2009). *The earth's ionosphere: Plasma physics and electrodynamics*. Academic press.

Kil, H., & Heelis, R. A. (1998a). Equatorial density irregularity structures at intermediate scales and their temporal evolution. *Journal of Geophysical Research: Space Physics*, *103*(A3), 3969-3981. doi: https://doi.org/10.1029/97JA03344

Kil, H., & Heelis, R. A. (1998b). Global distribution of density irregularities in the equatorial ionosphere. *Journal of Geophysical Research: Space Physics*, *103*(A1), 407-417. doi: https://doi.org/10.1029/97JA02698

Kil, H., Heelis, R. A., Paxton, L. J., & Oh, S.-J. (2009). Formation of a plasma depletion shell in the equatorial ionosphere. *Journal of Geophysical Research: Space Physics*, *114*(A11). doi: https://doi.org/10.1029/2009JA014369

Knudsen, D. J., Burchill, J. K., Buchert, S. C., Eriksson, A. I., Gill, R., Wahlund, J.-E., ... Moffat, B. (2017). Thermal ion imagers and Langmuir probes in the Swarm electric field instruments. *Journal of Geophysical Research: Space Physics*, *122*(2), 2655-2673. doi: https://doi.org/10.1002/2016JA022571

Kudeki, E., & Bhattacharyya, S. (1999). Postsunset vortex in equatorial F-region plasma drifts and implications for bottomside spread-F. *Journal of Geophysical Research: Space Physics*, *104*(A12), 28163-28170. doi: https://doi.org/10.1029/1998JA900111

Li, G., Ning, B., Otsuka, Y., Abdu, M. A., Abadi, P., Liu, Z., ... Wan, W. (2021, Jan 01). Challenges to Equatorial Plasma Bubble and Ionospheric Scintillation Short-Term Forecasting and Future Aspects in East and Southeast Asia. *Surveys in Geophysics*, *42*(1), 201-238. doi: https://doi.org/10.1007/s10712-020-09613-5

Lühr, H., Maus, S., Rother, M., & Cooke, D. (2002). First in-situ observation of night-time F region currents with the CHAMP satellite. *Geophysical Research Letters*, *29*(10), 127-1-127-4. doi: https://doi.org/10.1029/2001GL013845

Lühr, H., Rother, M., Maus, S., Mai, W., & Cooke, D. (2003). The diamagnetic effect of the equatorial appleton anomaly: Its characteristics and impact on geomagnetic field modeling. *Geophysical Research Letters*, *30*(17). doi: https://doi.org/10.1029/2003GL017407

Lühr, H., Xiong, C., Park, J., & Rauberg, J. (2014). Systematic study of intermediate-scale structures of equatorial plasma irregularities in the ionosphere based on CHAMP observations. *Frontiers in Physics*, *2*. doi: https://doi.org/10.3389/fphy.2014.00015

Macho, E. P., Correia, E., Spogli, L., & Tadeu de Assis Honorato Muella, M. (2022). Climatology of ionospheric amplitude scintillation on gnss signals at south american sector during solar cycle 24. *Journal of Atmospheric and Solar-Terrestrial Physics*, *231*, 105872. doi: https://doi.org/10.1016/j.jastp.2022.105872

Manju, G., & Aswathy, R. P. (2020). Ionospheric Planetary Wave Activity and Its Role in Equatorial Spread F Day-to-Day Variability. *Journal of Geophysical Research: Space Physics*, *125*(9), e2020JA027960. (e2020JA027960 2020JA027960) doi: https://doi.org/10.1029/2020JA027960

Martinis, C., Daniell, R., Eastes, R., Norrell, J., Smith, J., Klenzing, J., ... Burns, A. (2021). Longitudinal Variation of Postsunset Plasma Depletions From the Global-Scale Observations of the Limb and Disk (GOLD) Mission. *Journal of Geophysical Research: Space Physics*, *126*(2), e2020JA028510. doi: https://doi.org/10.1029/2020JA028510

Martinis, C., & Mendillo, M. (2007). Equatorial spread F-related airglow depletions at Arecibo and conjugate observations. *Journal of Geophysical Research: Space Physics*, *112*(A10). doi: https://doi.org/10.1029/2007JA012403

Mason, I. (1982). A Model for Assessment of Weather Forecasts. *Australian Meteorological Magazine*, *30*, 291-303.

Matzka, J., Bronkalla, O., Kervalishvili, G., Rauberg, J., Stolle, C., & Yamazaki, Y. (2022). *Geomagnetic Hpo index. V. 2.0.* [Dataset]. GFZ Data Services. doi: https://doi.org/10.5880/Hpo.0002

Murhy, A. H. (1993). What Is a Good Forecast? An Essay on the Nature of Goodness in Weather Forecasting. *Weather and Forecasting*, *8*(2), 281-293. doi: https://doi.org/10.1175/1520-0434(1993)008⟨0281:WIAGFA⟩2.0.CO;2

Murphy, J. M. (1988). The impact of ensemble forecasts on predictability. *Quarterly Journal of the Royal Meteorological Society*, *114*(480), 463-493. doi: https://doi.org/10.1002/qj.49711448010

Murray, S. A., Bingham, S., Sharpe, M., & Jackson, D. R. (2017). Flare forecasting at the Met Office Space Weather Operations Centre. *Space Weather*, *15*(4), 577–588. doi: https://doi.org/10.1002/2016SW001579

Nishizuka, N., Kubo, Y., Sugiura, K., Den, M., & Ishii, M. (2020). Reliable Probability Forecast of Solar Flares: Deep Flare Net-Reliable (DeFN-R). *The Astrophysical Journal*, *899*(2), 150. doi: 10.3847/1538-4357/aba2f2

Olsen, N., Friis-Christensen, E., Floberghagen, R., Alken, P., Beggan, C. D., Chulliat, A., ... Visser, P. N. (2013). The Swarm Satellite Constellation Application and Research Facility (SCARF) and Swarm data products. *Earth, Planets and Space*, *65*(11), 1189-1200. doi: https://doi.org/10.5047/eps.2013.07.001

Ossakow, S. L. (1981). Spread-F theories-A review. *Journal of Atmospheric and Terrestrial Physics*, *43*(5), 437-452. doi: https://doi.org/10.1016/0021-9169(81)90107

-0

Park, J., Noja, M., Stolle, C., & Lühr, H. (2013). The Ionospheric Bubble Index deduced from magnetic field and plasma observations onboard Swarm. *Earth, Planets and Space*, *65*(11), 1333-1344. doi: https://doi.org/10.5047/eps.2013.08.005

Patra, A. K., & Das, S. K. (2023). On the Upwelling of the F Layer Base and Prediction of Equatorial Plasma Bubble. *Geophysical Research Letters*, *50*(7), e2023GL102803. doi: https://doi.org/10.1029/2023GL102803

Rajesh, P. K., Lin, C. C. H., Chen, C. H., Chen, W. H., Lin, J. T., Chou, M. Y., ... You, C. F. (2017). Global equatorial plasma bubble growth rates using ionosphere data assimilation. *Journal of Geophysical Research: Space Physics*, *122*(3), 3777-3787. doi: https://doi.org/10.1002/2017JA023968

Reddy, S. A., Forsyth, C., Aruliah, A., Smith, A., Bortnik, J., Aa, E., ... Lewis, G. (2023). Predicting Swarm Equatorial Plasma Bubbles via Machine Learning and Shapley Values. *Journal of Geophysical Research: Space Physics*, *128*(6), e2022JA031183. doi: https://doi.org/10.1029/2022JA031183

Reigber, C., Lühr, H., & Schwintzer, P. (2002). CHAMP mission status. *Advances in Space Research*, *30*(2), 129-134. doi: https://doi.org/10.1016/S0273-1177(02)00276-4

Retterer, J. M., & Roddy, P. (2014). Faith in a seed: on the origins of equatorial plasma bubbles. *Annales Geophysicae*, *32*(5), 485–498. doi: https://doi.org/10.5194/angeo-32-485-2014

Rodríguez-Zuluaga, J., Stolle, C., Yamazaki, Y., Lühr, H., Park, J., Scherliess, L., & Chau, J. L. (2019). On the Balance Between Plasma and Magnetic Pressure Across Equatorial Plasma Depletions. *Journal of Geophysical Research: Space Physics*, *124*(7), 5936-5944. doi: https://doi.org/10.1029/2019JA026700

Rother, M., & Michaelis, I. (2019). *CH-ME-3-MAG - CHAMP 1 Hz Combined Magnetic Field Time Series (Level 3)* [Dataset]. GFZ Data Services. doi: https://doi.org/10.5880/GFZ.2.3.2019.004

Sahai, Y., Aarons, J., Mendillo, M., Baumgardner, J., Bittencourt, J., & Takahashi, H. (1994). OI 630 nm imaging observations of equatorial plasma depletions at 16° S dip latitude. *Journal of Atmospheric and Terrestrial Physics*, *56*(11), 1461-1475. doi: https://doi.org/10.1016/0021-9169(94)90113-9

Sahai, Y., Fagundes, P., & Bittencourt, J. (2000). Transequatorial F-region ionospheric plasma bubbles: solar cycle effects. *Journal of Atmospheric and Solar-Terrestrial Physics*, *62*(15), 1377-1383. doi: https://doi.org/10.1016/S1364-6826(00)00179-6

Saito, S., & Maruyama, T. (2006). Ionospheric height variations observed by ionosondes along magnetic meridian and plasma bubble onsets. *Annales Geophysicae*, *24*(11), 2991–2996. doi: https://doi.org/10.5194/angeo-24-2991-2006

Saito, S., & Maruyama, T. (2007). Large-scale longitudinal variation in ionospheric height and equatorial spread F occurrences observed by ionosondes. *Geophysical Research Letters*, *34*(16). doi: https://doi.org/10.1029/2007GL030618

Sheather, S. J., & Jones, M. C. (1991). A Reliable Data-Based Bandwidth Selection Method for Kernel Density Estimation. *Journal of the Royal Statistical Society: Series B (Methodological)*, *53*(3), 683-690. doi: https://doi.org/10.1111/j.2517-6161.1991.tb01857.x

Shinagawa, H., Jin, H., Miyoshi, Y., Fujiwara, H., Yokoyama, T., & Otsuka, Y. (2018). Daily and seasonal variations in the linear growth rate of the Rayleigh-Taylor instability in the ionosphere obtained with GAIA. *Progress in Earth and Planetary Science*, *5*(1), 16. doi: https://doi.org/10.1186/s40645-018-0175-8

Singh, S., Johnson, F. S., & Power, R. A. (1997). Gravity wave seeding of equatorial plasma bubbles. *Journal of Geophysical Research: Space Physics*, *102*(A4), 7399-7410. doi: https://doi.org/10.1029/96JA03998

Stolle, C., Lühr, H., & Fejer, B. G. (2008). Relation between the occurrence rate of ESF and the equatorial vertical plasma drift velocity at sunset derived from global observations. *Annales Geophysicae*, *26*(12), 3979–3988. doi: https://doi.org/10.5194/angeo-26-3979-2008

Stolle, C., Lühr, H., Rother, M., & Balasis, G. (2006). Magnetic signatures of equatorial spread F as observed by the CHAMP satellite. *Journal of Geophysical Research: Space Physics*, *111*(A2). doi: https://doi.org/10.1029/2005JA011184

Su, S.-Y., Chao, C. K., & Liu, C. H. (2008). On monthly/seasonal/longitudinal variations of equatorial irregularity occurrences and their relationship with the post-sunset vertical drift velocities. *Journal of Geophysical Research: Space Physics*, *113*(A5). doi: https://doi.org/10.1029/2007JA012809

Su, S.-Y., Yeh, H. C., & Heelis, R. A. (2001). ROCSAT 1 ionospheric plasma and electrodynamics instrument observations of equatorial spread F: An early transitional scale result. *Journal of Geophysical Research: Space Physics*, *106*(A12), 29153-29159. doi: https://doi.org/10.1029/2001JA900109

Sultan, P. J. (1996). Linear theory and modeling of the Rayleigh-Taylor instability leading to the occurrence of equatorial spread F. *Journal of Geophysical Research: Space Physics*, *101*(A12), 26875-26891. doi: https://doi.org/10.1029/96JA00682

Swets, J. A. (1973). The Relative Operating Characteristic in Psychology: A technique for isolating effects of response bias finds wide use in the study of perception and cognition. *Science*, *182*(4116), 990–1000.

Tapping, K. F. (2013). The 10.7cm solar radio flux (f10.7). *Space Weather*, *11*(7), 394-406. doi: https://doi.org/10.1002/swe.20064

Tsunoda, R. T. (2005). On the enigma of day-to-day variability in equatorial spread F. *Geophysical Research Letters*, *32*(8). doi: https://doi.org/10.1029/2005GL022512

Tsunoda, R. T., Bubenik, D. M., Thampi, S. V., & Yamamoto, M. (2010). On large-scale wave structure and equatorial spread F without a post-sunset rise of the F layer. *Geophysical Research Letters*, *37*(7). doi: https://doi.org/10.1029/2009GL042357

Tsunoda, R. T., Saito, S., & Nguyen, T. T. (2018). Post-sunset rise of equatorial F layer—or upwelling growth? *Progress in Earth and Planetary Science*, *5*(1), 22. doi: https://doi.org/10.1186/s40645-018-0179-4

Tsunoda, R. T., & White, B. R. (1981). On the generation and growth of equatorial backscatter plumes 1. Wave structure in the bottomside F layer. *Journal of Geophysical Research: Space Physics*, *86*(A5), 3610-3616. doi: https://doi.org/10.1029/JA086iA05p03610

Wheatland, M. S. (2005). A statistical solar flare forecast method. *Space Weather*, *3*(7). doi: https://doi.org/10.1029/2004SW000131

Wilks, D. (1995). *Forecast verification. Statistical methods in the atmospheric sciences.* Academic Press New York, NY, USA.

Woodman, R. F., & La Hoz, C. (1976). Radar observations of F region equatorial irregularities. *Journal of Geophysical Research (1896-1977)*, *81*(31), 5447-5466. doi: https://doi.org/10.1029/JA081i031p05447

Xiong, C., Park, J., Lühr, H., Stolle, C., & Ma, S. Y. (2010). Comparing plasma bubble occurrence rates at CHAMP and GRACE altitudes during high and low solar activity. *Annales Geophysicae*, *28*(9), 1647–1658. Retrieved from `https://angeo.copernicus.org/articles/28/1647/2010/` doi: 10.5194/angeo-28-1647-2010

Xiong, C., Stolle, C., & Lühr, H. (2016). The Swarm satellite loss of GPS signal and its relation to ionospheric plasma irregularities. *Space Weather*, *14*(8), 563-577. Retrieved from `https://agupubs.onlinelibrary.wiley.com/doi/abs/10.1002/2016SW001439` doi: https://doi.org/10.1002/2016SW001439

Xiong, C., Xu, J.-S., Stolle, C., van den Ijssel, J., Yin, F., Kervalishvili, G. N., & Zangerl, F. (2020). On the Occurrence of GPS Signal Amplitude Degradation for

Receivers on Board LEO Satellites. *Space Weather*, *18*(2), e2019SW002398. doi: https://doi.org/10.1029/2019SW002398

Yamamoto, M., Otsuka, Y., Jin, H., & Miyoshi, Y. (2018). Relationship between day-to-day variability of equatorial plasma bubble activity from GPS scintillation and atmospheric properties from Ground-to-topside model of Atmosphere and Ionosphere for Aeronomy (GAIA) assimilation. *Progress in Earth and Planetary Science*, *5*(1), 26. doi: https://doi.org/10.1186/s40645-018-0184-7

Yamazaki, Y., Matzka, J., Stolle, C., Kervalishvili, G., Rauberg, J., Bronkalla, O., ... Jackson, D. R. (2022). Geomagnetic Activity Index Hpo. *Geophysical Research Letters*, *49*(10), e2022GL098860. doi: https://doi.org/10.1029/2022GL098860

Zhan, W., Rodrigues, F. S., & Milla, M. A. (2018). On the Genesis of Postmidnight Equatorial Spread F: Results for the American/Peruvian Sector. *Geophysical Research Letters*, *45*(15), 7354-7361. doi: https://doi.org/10.1029/2018GL078822